CHALMERS
UNIVERSITY OF TECHNOLOGY

High temperature corrosion behavior of FeCrAlSi model alloys in the presence of water vapor and KCl at 600 °C – The influence of Cr content

Downloaded from: https://research.chalmers.se, 2022-07-02 09:28 UTC

Citation for the original published paper (version of record):
Eklund, J., Hanif, I., Bigdeli, S. et al (2022). High temperature corrosion behavior of FeCrAlSi model alloys in the presence of water vapor and
KCl at 600 °C – The influence of Cr content. Corrosion Science, 198.
http://dx.doi.org/10.1016/j.corsci.2022.110114

N.B. When citing this work, cite the original published paper.

research.chalmers.se offers the possibility of retrieving research publications produced at Chalmers University of Technology.
It covers all kind of research output: articles, dissertations, conference papers, reports etc. since 2004.
research.chalmers.se is administrated and maintained by Chalmers Library

(article starts on next page)

Corrosion Science 198 (2022) 110114

Contents lists available at ScienceDirect

Corrosion Science

journal homepage: www.elsevier.com/locate/corsci

High temperature corrosion behavior of FeCrAlSi model alloys in the presence of water vapor and KCl at 600 °C – The influence of Cr content

J. Eklund *, I. Hanif, S. Bigdeli, T. Jonsson

Energy and Materials, Department of Chemistry and Chemical Engineering, Chalmers University of Technology, S-412 96 Göteborg, Sweden

ARTICLE INFO

Keywords:
A. FeCrAl
A. Chromium
A. Silicon
B. STEM
C. High temperature corrosion
C. Internal oxidation

ABSTRACT

The corrosion behavior of Fe(5−20)Cr3Al2Si model alloys and the underlying mechanisms after breakaway oxidation was investigated at 600 °C. Rapid breakaway oxidation was triggered for all alloys in the presence of KCl(s). Thermogravimetric analysis showed that alloys with a Cr content of ≥ 10 wt% transitioned into sub-parabolic oxidation kinetics at an early stage of the oxidation process after breakaway oxidation. Through advanced electron/ion microscopy, this behavior was attributed to high Cr-enrichment in the bottom part of the inward-growing scale, indicating the formation of a healing layer. Additionally, alloys with elevated Cr-content (≥15 wt%) were more prone to grain boundary attack.

1. Introduction

The corrosion resistance of FeCrAl alloys have been studied extensively at high temperatures (900–1300 °C) at which they are known to form a protective α-alumina scale, attributing to their excellent corrosion resistance [1–3]. Because of the protective α-alumina scale in this temperature range, FeCrAl alloys are commonly used as heating elements for various applications, for example the electrical elements of gas burners, furnace rollers and ignitors. FeAl alloys may also form an α-alumina scale but it has been shown that addition of Cr to the alloy reduces the amount of Al needed to form this protective layer [4].

Below approximately 900 °C, the kinetics for the formation of α-alumina is slower and less protective transient allotropes of alumina instead forms in the initial stages of the oxidation process. Therefore, chromia-forming stainless steels are normally used at lower temperatures, at which they are able to form a protective chromia scale. However, these protective oxide scales tend to break down in highly corrosive environments, such as biomass- and waste-fired boilers which generally contain large amounts of alkali salts and water vapor. In the presence of these species, the protective chromia scale has been suggested to break down through two separate mechanisms: Cr evaporation due to volatilization of chromium-oxy-hydroxide in the presence of water vapor [5]; and reaction with alkali salts, leading to the formation of alkali chromates [6–10]. The loss of the chromia scale, which can be considered the primary protection of the alloy [11], is usually followed by the formation of fast-growing Fe-rich oxide, resulting in rapid material degradation and high maintenance costs. FeCrAl alloys, for which the primary protection is alumina, may be used to prevent the breakdown of the primary protection in this type of environment. However, many critical components in the biomass-and waste-fired boilers are exposed to temperatures below 900 °C which may negatively influence the properties of the primary protection of FeCrAl alloys. Previous studies have shown that FeCrAl alloys may form a thin protective transient alumina scale at 600 °C [12] which contains significant amounts of both Fe and Cr [13], making them sensitive towards the presence of alkali chlorides (leading to breakaway oxidation).

Retaining the primary protection in harsh environments is thus very challenging during long-term operation. Instead, another approach, associated with a reduced dependence on the primary protection, has recently been investigated [11]. The approach is based on improving the protectiveness of the Fe-rich oxide, i.e., the secondary protection of the alloy, by reducing the oxide scale growth rate. It is in this context very important to understand how different alloying elements influence the secondary protection, i.e., growth kinetics following breakaway corrosion. Studies of the secondary protection and the influence of alloying elements are very limited. The corrosion behavior of an Fe10Cr4Al alloy with minor additions of Si was exposed in a harsh environment and was investigated in detail in [14]. It was shown that Si significantly improves the secondary protection, by reducing the growth rate of the Fe-rich oxide scale. The same trend was observed when exposing similar alloys in a waste-fired boiler [15]. In addition, Persdotter et al. demonstrated the possibility of improving the secondary protection by

* Corresponding author.
E-mail address: johekl@chalmers.se (J. Eklund).

https://doi.org/10.1016/j.corsci.2022.110114
Received 25 October 2021; Received in revised form 17 January 2022; Accepted 19 January 2022
Available online 22 January 2022
0010-938X/© 2022 The Author(s). Published by Elsevier Ltd. This is an open access article under the CC BY license (http://creativecommons.org/licenses/by/4.0/).

increasing the amounts of Cr and Al and indications of synergistic interactions between these [11]. These effects were further investigated by Eklund et al. [16] which showed that the growth rate of the Fe-rich oxide scale was significantly reduced for FeCrAl alloys when exceeding a Cr content of 18 wt% whereas the FeCrAl alloys with a Cr content below this critical limit and all investigated FeCr alloys displayed oxidation kinetics similar to pure Fe. This effect was attributed to the prevention of internal oxidation, enabling the formation of a healing layer at the metal oxide interface which was in agreement with thermodynamic calculations. Because of the previously observed effect of Si, investigating the influence of Cr on the secondary protection kinetics and microstructure of Si-containing FeCrAl alloys is of great interest.

The aim of the present work is to investigate the influence of Cr content on the secondary protection of Si-containing FeCrAl alloys at 600 °C. FeCrAlSi model alloys with varying Cr content have been isothermally exposed in oxygen and water vapor with and without KCl present on the sample surface at 600 °C in a tube furnace. The same alloys have also been exposed in a thermobalance under the same conditions in order to study the kinetics of the corrosion process. Detailed microstructural investigations of the corrosion products were performed using SEM/EDX, FIB/SEM, SEM/EBSD and STEM/EDX. In addition, thermodynamic calculations were used, in a methodological way similar to [16], to gain more insight about the possible mechanisms involved.

2. Experimental procedure

2.1. Sample preparation

Four different FeCrAl model alloys, with varying Cr content, were used in this study (compositions of the alloys are shown in Table 1). The model alloys were produced by melting the material in a vacuum induction furnace into a 1 kg ingot. This ingot was then hot-rolled into a strip and further machined to achieve a thickness of roughly 2 mm. The strip was later heat treated at 950 °C to achieve a uniform grain size distribution. The strip was cut into coupons with a dimension of 10 × 12 mm. A small hole with a diameter of 1.5 mm was drilled into the sample to simplify the weighing. A second heat treatment, also at 950 °C, was performed to relax elongated grains in the bulk of the samples. Prior to exposure, the sample coupons were ground with P500 to P4000 SiC paper and polished down to 1 μm with a diamond suspension until a mirror-like surface was achieved.

2.2. Exposure

The samples were weighed using a Sartorius™ balance with microgram resolution prior to exposure. After weighing, KCl was deposited on the surface of the samples by spraying a water-ethanol (20:80) solution saturated with KCl. A continuous flow of warm air was directed towards the sample during spraying to accelerate the drying of the solution. After spraying, the samples were weighed again to determine the amount of KCl deposited on the sample. The procedure was repeated until an amount of 1 mg/cm^2 was deposited on the samples.

Two types of exposures were performed in this study, using a horizontal silica tube furnace and a thermobalance. The tube furnace exposures were performed with a flow rate of 3 cm/s (calibrated by a Bios Definer 220 M) and a gas composition of 5%O_2 + 20%H_2O + N_2 (Bal.) at 600 °C for 168 h. Reference exposures without KCl present were also performed in the tube furnace. Samples were mounted vertically in alumina sample holders in the same direction as the tube furnace. After the exposure the samples were weighed to measure the mass gain. The thermobalance exposures were performed with a Setaram Evolution equipped with a Setaram Wetsys (to generate the desired humidity for the exposures). These exposures were performed in a similar environment but with a lower flow rate (about 1.5 cm/s) in the thermobalance. The thermobalance exposures were only performed with KCl deposited on the samples. The samples were weighed before and after the thermobalance exposures to ensure that the correct mass gain had been recorded. Only one sample could be exposed at a time in the thermobalance and the exposures were therefore repeated at least three times to ensure reproducibility.

Table 1
Nominal composition (wt%) of FeCrAl model alloys.

Alloy	Fe	Cr	Al	Si	Other elements
Fe**5Cr**AlSi	Bal.	5	3	2	C, N, Zr
Fe**10Cr**AlSi	Bal.	10	3	2	
Fe**15Cr**AlSi	Bal.	15	3	2	
Fe**20Cr**AlSi	Bal.	20	3	2	

KCl has been found to evaporate at a fast rate under the present exposure conditions [17]. Because of this, the recorded mass gain may be lower than the actual mass gain (from oxide formation) due to the loss of KCl. However, from knowing the rate of KCl evaporation it is possible to estimate the actual mass gain (due to oxide formation). For this reason, the rate of KCl evaporation was measured by depositing 1 mg/cm^2 KCl on gold coupons and subsequent exposure in tube furnace and thermobalance. The evaporation rate of KCl was found to be roughly 0.03 mg/cm^2 h in the tube furnace and 0.008 mg/cm^2 h in the thermobalance. Since Cr is known to evaporate under the present conditions, a point of concern is whether it is accurate to assume that KCl evaporation is the only phenomenon responsible for reducing the mass gain. However, previous reports have shown that 0.01 mg/cm^2 of Cr had evaporated from a chromia former after 90 h of exposure under similar conditions [18] while 0.001 mg/cm^2 of Cr had evaporated from a Fe10Cr4Al2Si alloy after 168 h [19]. The Cr-evaporation can therefore be considered negligible.

2.3. Analysis

Cross sections of the exposed samples were prepared by attaching a thin Si wafer onto the sample surface using Loctite 415 glue. After the glue had dried for about 24 h the samples were dry cut with a low-speed diamond saw and subsequently milled using a Leica TIC 3X broad ion beam (BIB) instrument to achieve a smooth surface for more detailed microstructural analysis. The three argon ion beam guns of the BIB instrument were operated at 6.5 kV for 10–14 h (depending on the total operating time of the argon guns).

The composition and morphology of the oxide scales were investigated by analyzing both the plan view and the cross sections of the exposed samples with scanning electron microscopy (SEM) using both backscattered electrons (BSE) and secondary electrons (SE). An FEI Quanta 200 SEM equipped with an Oxford Instruments X-Max^N 80 T energy dispersive X-ray (EDX) detector was used for the SEM analysis in this work.

Electron Backscattered Diffraction (EBSD) analysis was carried out for phase determination using a TESCAN GAIA3 dual beam FIB-SEM instrument equipped with an Oxford Instruments Nordlys detector. Since the sample surface plays a vital role for EBSD analysis, already BIB milled cross sections (at 6.5 – 8 kV) were additionally BIB milled at 4 kV for 4 h and subsequently milled at 2 kV for 4 h to remove the ion beam induced damages e.g., reduce the amorphous layer. The prepared samples were then mounted on a 20 degrees pre-tilted holder such that the angle between the electron beam and the sample (cross-section) was 70 degrees for analytical analysis. The microscope was operated at 20 kV for all EBSD analysis while beam current and camera exposure was suitably adjusted to attain sharp diffraction patterns for phase determination using the Aztec live software.

Focused Ion beam (FIB) milling was used to prepare thin lamellae for transmission electron microscopy (TEM) using an FEI Versa 3D dual beam machine equipped with a gas injection system (GIS) and an Oxford Instrument's Omniprobe needle. The thin lamellae were prepared from BIB milled cross sections, covering the outward and inward growing

oxide layers along with a minor part of the material substrate for detailed investigation. Typical TEM sample preparation was employed, and the thin lamellae were lifted out using the Omniprobe needle and subsequently attached to a TEM Cu-grid where it was thinned down to approximately 100 nm.

The TEM analysis in this study was performed with an FEI Titan 80–300 transmission electron microscope (TEM) equipped with an Oxford Instruments INCA X-sight EDX detector. The microscope was operated in scanning TEM (STEM) and TEM mode under different conditions. STEM-EDX analysis was performed to determine the chemical compositions and elemental distribution within the sample through point analysis and line scans. High-angle annular dark field (HAADF) imaging was also performed in STEM mode. In addition, convergent beam electron diffraction (CBED) patterns were obtained in TEM mode for phase determination.

3. Results

3.1. Gravimetry

3.1.1. Tube furnace

After exposure for 168 h in the absence of KCl, all model alloys displayed very low mass gains, see Fig. 1. This indicates that all alloys managed to retain the primary protection, i.e., formation of thin protective oxide scales in the 50–100 nanometer range. Increasing the Cr content resulted in a slight decrease in mass gain.

After exposure in the presence of KCl for 168 h, most of the alloys exhibited much higher mass gains compared to those exposed in the absence of KCl. This indicates breakaway oxidation, i.e., transition into the secondary corrosion regime, see Fig. 1. The Fe**5Cr**AlSi alloy exhibited the highest mass gain, i.e., 4.25 mg/cm^2 which corresponds to a theoretical oxide thickness of 26 μm. Increasing the Cr content in the model alloys resulted in lower mass gains. The Fe**10Cr**AlSi alloy displayed a mass gain of 1.37 mg/cm^2 which corresponds to a theoretical oxide thickness of 8.3 μm while the Fe**15Cr**AlSi alloy displayed further reduction in mass gain with a value of 0.43 mg/cm^2 which corresponds to a theoretical oxide thickness of 2.6 μm. The Fe**20Cr**AlSi alloy displayed a negative mass gain value after exposure which is attributed to the high evaporation rate of KCl (see exposure section). The high evaporation of KCl must be considered for each of the alloys when evaluating the mass gains since the actual mass gain (from oxide formation) can be considered to be higher than the recorded mass gains.

3.1.2. Thermobalance

In order to investigate the initial oxidation kinetics in the presence of KCl the model alloys were exposed in a thermobalance for 48 h. The solid curves in Fig. 2 correspond to the weight change recorded by the thermobalance. Initially, the Fe**15Cr**AlSi and Fe**20Cr**AlSi alloys displayed a mass gain during the first 24 and 6 h of the exposures

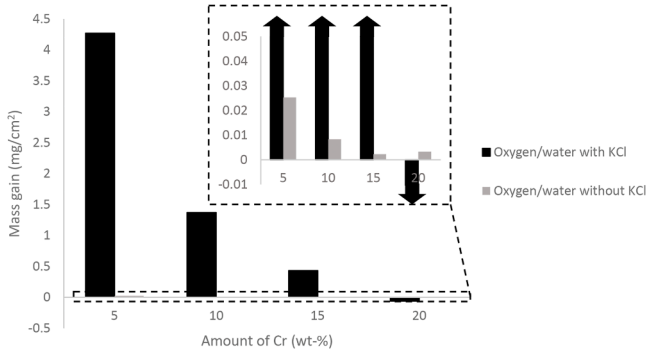

Fig. 1. Mass gains of alloys exposed to 5% O_2 + 20% H_2O + N_2 (Bal.) at 600 °C with and without KCl present in a tube furnace for 168 h.

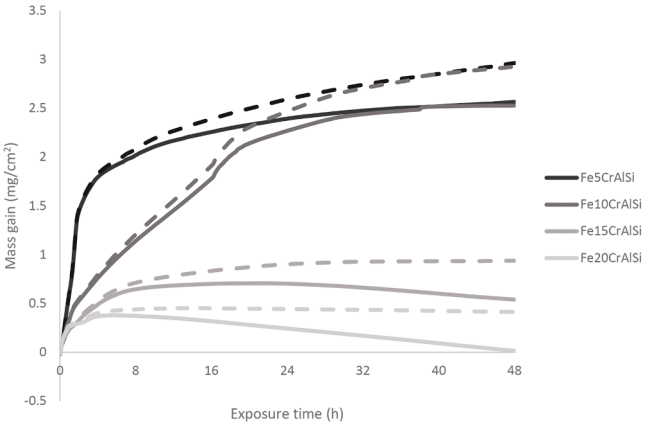

Fig. 2. Kinetic behavior of the alloys exposed to 5% O_2 + 20% H_2O at 600 °C with KCl present in a thermobalance for 48 h. The dashed curves are adjusted according to mass loss due to the evaporation of KCl under the present conditions.

respectively, followed by a mass loss. The mass loss is interpreted to be caused by the high evaporation rate of KCl under the given conditions, i.e., a mass loss is caused by the evaporation being higher than the corrosion rate for Fe**15Cr**AlSi and Fe**20Cr**AlSi after 24 and 6 h of exposure, respectively. In order to remove the contribution of KCl evaporation on the mass gain curves, these were adjusted by adding a mass gain, compensating the expected KCl evaporation to the weight recorded by the thermobalance. The adjusted behavior is displayed as dashed curves in Fig. 2. The α-value, i.e., the exponent in the relationship between the mass gain and time ($m^{\alpha} \propto t$), was calculated from the mass gain curves, adjusted with respect to the KCl evaporation, for different time intervals in which the kinetics differed, see Table 2.

The thermobalance results displayed high mass gain for all alloys during the first two hours of the exposures, indicating breakaway oxidation and a transition from the primary to the secondary regime. However, the oxidation kinetics of the corrosion process differed significantly between the alloys. The oxidation rate of the Fe**5Cr**AlSi alloy was initially high during the first two hours (giving an α-value less than 1), reaching a mass gain of roughly 1.5 mg/cm^2 but was then rapidly reduced and transitioned into a sub-parabolic behavior (α-value of 5). The final mass gain of Fe**5Cr**AlSi was 2.5 mg/cm^2 according to the recorded mass gain and 3.3 mg/cm^2 for the adjusted mass gain, which corresponds to theoretical oxide thicknesses of 17.5 μm and 23 μm respectively (calculations based on the assumption that only magnetite forms). The Fe**10Cr**AlSi alloy displayed a rapid initial oxidation rate (first hour with an α-value of 1.5) followed by a reduced oxidation rate due to a transition into parabolic behavior (α-value of 2) for 15 h. The oxidation rate increased for a short amount of time after 16 h of exposure, indicating possible crack formation, followed by a transition into sub-parabolic behavior (α-value of 4). This resulted in a final mass gain of 2.5 mg/cm^2 according to the recorded mass gain and 3.3 mg/cm^2 for the corrected mass gain which corresponds to theoretical oxide

Table 2
α-values for different time intervals during exposure of each of the investigated alloys. The values are calculated based on the corrected behaviors (dashed curves) in Fig. 2.

Fe5CrAlSi	0–2 h	2–48 h		
α	< 1	5		
Fe10CrAlSi	0–0.5 h	0.5–16 h	16–48 h	
α	1.5	2	4	
Fe15CrAlSi	0–10 h	10–30 h	30–48 h	
α	2	5	50	
Fe20CrAlSi	0–0.5 h	0.5–5 h	5–13 h	13–48
α	2	5	14	-14

thicknesses of 17.5 μm and 23 μm respectively. The Fe**15Cr**AlSi alloy displayed a parabolic behavior during the first 10 h of the exposure (α-value of 2) followed by a transition into sub-parabolic behavior. During the last 18 h of the exposure, the Fe**15Cr**AlSi alloy displayed a very high α-value (α-value of 50). As previously mentioned, due to the high evaporation rate of KCl, Fe**15Cr**AlSi exhibited mass loss after about 24 h of exposure which resulted in a final mass gain of roughly 0.5 mg/cm^2, corresponding to a theoretical oxide thickness of 3.5 μm. However, by considering the evaporation of KCl, the adjusted mass gain data did not display a mass loss and resulted in a final mass gain of about 1.3 mg/cm^2. This mass gain corresponds to a theoretical oxide thickness of 9 μm. The Fe**20Cr**AlSi alloy displayed a parabolic behavior (α-value of 2) during the first hour of exposure, followed by a transition into sub-parabolic behavior (α-value of 5). An additional kinetic transition occurred after 5 h at which the order of parabolicity was further increased (α-value of 14). After 13 h of exposure, the Fe**20Cr**AlSi alloy displayed a negative α-value (α-value of −14), indicating that the rate of KCl evaporation is slightly underestimated. The Fe**20Cr**AlSi alloy exhibited a recorded final mass gain close to 0 mg/cm^2. However, adjusting the mass gain according to the recorded rate of KCl evaporation, resulted in a final mass gain of about 0.8 mg/cm^2, which corresponds to a theoretical oxide thickness of 5.5 μm.

3.2. Oxide morphology

All four alloys displayed smooth surfaces with only minor surface features after exposure in $O_2 + H_2O$, see Fig. 3. This indicates that all alloys were still in the primary corrosion regime. The Fe**5Cr**AlSi alloy has formed small Fe oxide nodules, sparsely dispersed on the surface. The Fe oxide nodules seem to originate from protruding zirconia particles present on the surface. Apart from the Fe oxide nodules, the surface is covered by a thin oxide scale (in the nanometer range) indicated by the alloy grains being distinguishable through the oxide scale in the SEM-BSE images. The other alloys do not display any surface features other than the zirconia particles and have formed thin oxide scales (primary protection), which is in line with the recorded mass gain.

After exposure in the presence of KCl, all alloys displayed rough surface morphologies and alloy grains were no longer visible through the oxide scales, see Fig. 4. This indicates the formation of a thick Fe-rich oxide scale and a transition from the primary to the secondary corrosion regime, which agrees with the thermogravimetrical analysis. For all alloys, except the Fe**5Cr**AlSi alloy, K_2CrO_4 is visible on the surface (identified by SEM/EDX and XRD) and the amount of K_2CrO_4 increased with the Cr content of the alloy. The Fe**5Cr**AlSi alloy displays a relatively smooth surface morphology compared to the other alloys with only minor surface features, such as overgrown unreacted KCl particles.

3.3. Oxide microstructure

The focus of this work was the influence of Cr on the oxidation behavior in harsh environments and the microstructural investigation was therefore performed on the alloys exposed in the presence of KCl(s). SEM-BSE cross sections were ion milled using Broad Ion Beam (BIB) milling to investigate the oxide microstructure in detail. The slow-growing scales formed on the Fe**15Cr**AlSi and Fe**20Cr**AlSi alloys were in addition investigated in detail using TEM.

3.3.1. Alloy Fe5CrAlSi (KCl)

Fig. 5 shows SEM-BSE cross section images of the Fe**5Cr**AlSi alloy after exposure in a thermobalance for 48 h (Fig. 5a) and a tube furnace for 168 h (Fig. 5b). After 48 h of exposure in the thermobalance, the Fe**5Cr**AlSi alloy displayed a 12–15 μm thick oxide scale consisting of a 5–7 μm thick outward-growing Fe oxide and a 7 μm thick inward-growing (Fe, Cr, Al Si)-oxide, see Fig. 5a. However, about 6 μm of

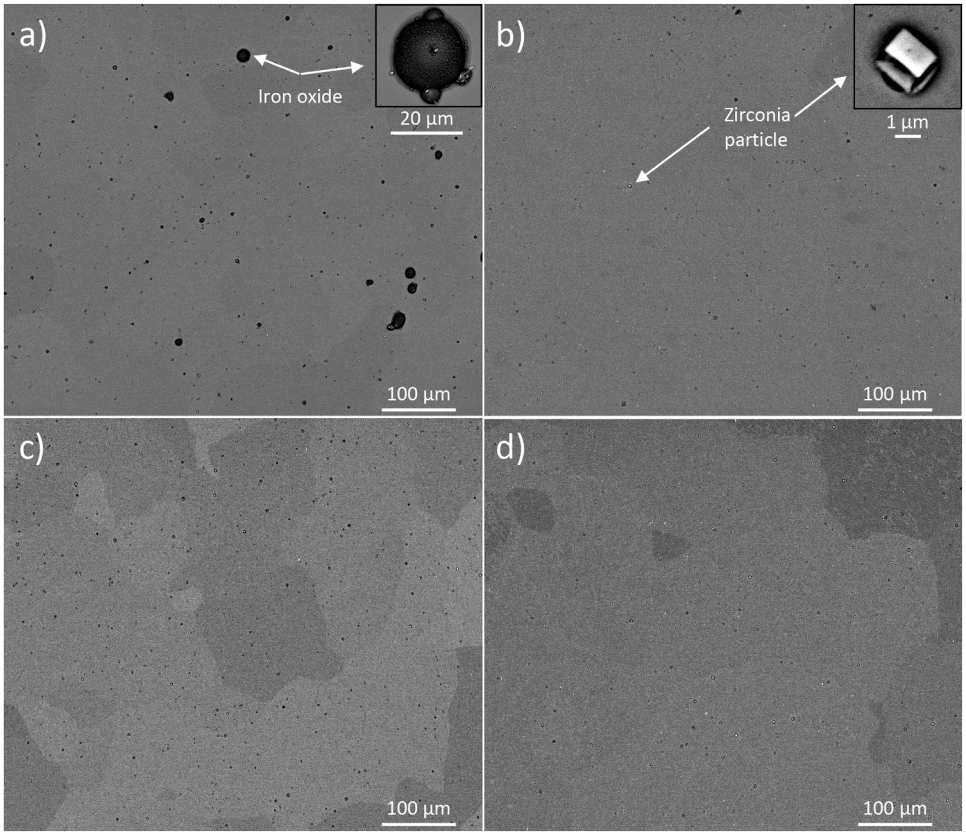

Fig. 3. SEM-BSE plan view images of a) Fe**5Cr**AlSi, b) Fe**10 C**rAlSi, c) Fe**15Cr**AlSi, and d) Fe**20Cr**AlSi after exposure to 5% O_2 + 20% H_2O at 600 °C for 168 h in a tube furnace.

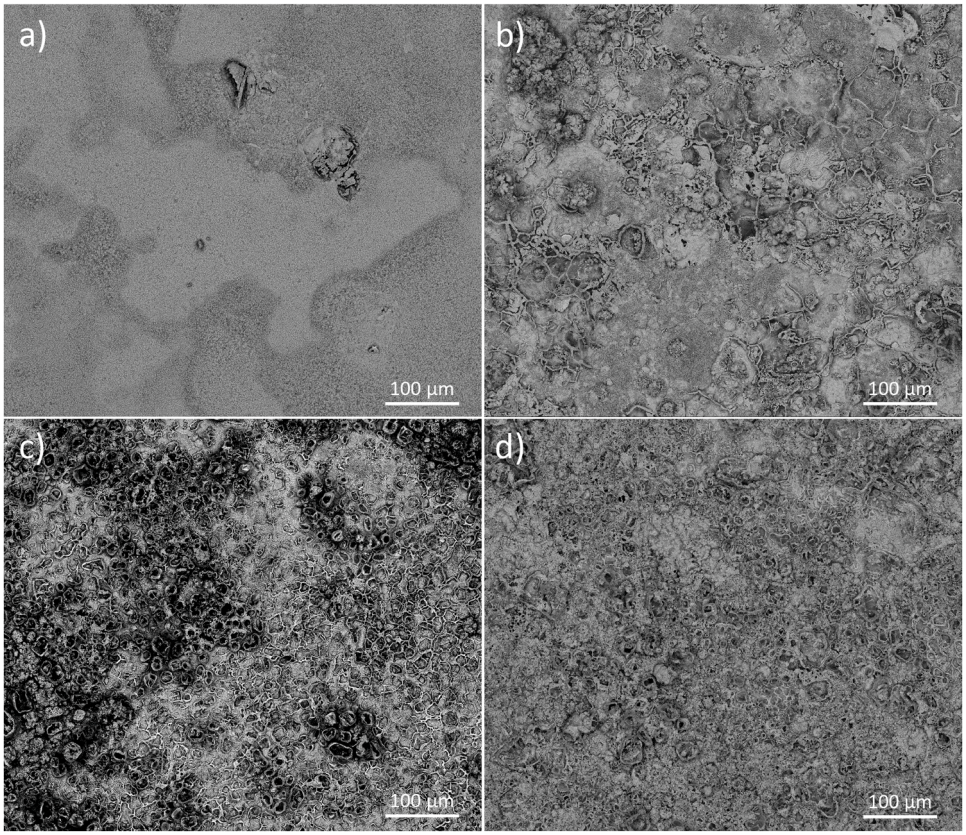

Fig. 4. SEM-BSE plan view image of a) Fe**5Cr**AlSi, b) Fe**10 C**rAlSi, c) Fe**15Cr**AlSi, and d) Fe**20Cr**AlSi after being exposed to 5% O_2 + 20% H_2O at 600 °C with KCl present in a tube furnace for 168 h.

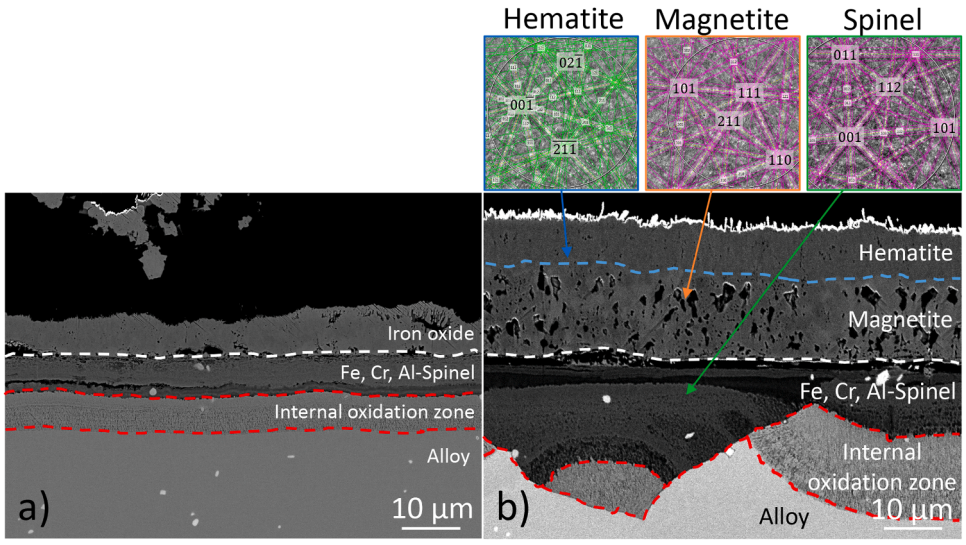

Fig. 5. SEM-BSE cross section images of Fe**5Cr**AlSi after being exposed to 5% O_2 + 20% H_2O at 600 °C with KCl present in a) a thermobalance for 48 h and b) a tube furnace for 168 h. The EBSD patterns in the blue, orange and green boxes (left to right) confirms the presence of hematite, magnetite and spinel respectively. (For interpretation of the references to colour in this figure legend, the reader is referred to the web version of this article.)

outward-growing oxide scale detached during sample preparation. The detached scale can be observed in the upper part of Fig. 5a. During the 168 h exposure in the tube furnace, the Fe**5Cr**AlSi alloy formed a 30–45 µm thick oxide scale consisting of a 23 µm thick outward-growing Fe oxide and a 6–22 µm inward-growing (Fe, Cr, Al, Si)-oxide, see Fig. 5. The outward-growing oxide consists of two layers, distinguished by the difference in contrast. From EBSD, the outer and inner Fe oxide layers were identified as hematite and magnetite respectively (see EBSD patterns included in Fig. 5). The SEM/BSE imaging of the inward growing scale indicate different layers by the difference in image contrast. This was verified by SEM/EDX-analysis showing an enrichment in Cr (20 at %), Al (25 at%) and Si (20 at%) and a depletion in Fe (40 at%) in the dark contrast areas while the brighter contrast areas were enriched in Fe (66 at%) with slightly lower Cr-, Al- and Si-contents (10, 15 and 10 at%

respectively). The presence of spinel was in addition identified by EBSD in the homogeneously thick inward-growing scale, see inserted Kikuchi pattern in Fig. 5. The contrast beneath the oxide scale and EDX analysis indicate that an internal oxidation zone has formed [20–22]. The SEM/BSE image shows that it has a discontinuous nature and is 10–15 μm thick.

3.3.2. Alloy Fe10CrAlSi (KCl)

Fig. 6 shows SEM-BSE cross section images of the Fe**10Cr**AlSi alloy after exposure in a thermobalance for 48 h (Fig. 6a) and a tube furnace for 168 h (Fig. 6b). After 48 h of exposure in the thermobalance, the Fe**10Cr**AlSi alloy formed a non-uniform oxide scale with highly varying thickness. The oxide scale shown in Fig. 6a represents the average oxide thickness (about 13 μm) while the observed oxide scale thickness varies over the surface in the range 3–85 μm. The microstructure displayed in Fig. 6a is similar to that of the Fe**5Cr**AlSi alloy with a 7–9 μm outward-growing Fe oxide scale and a 4–6 μm thick inward-growing (Fe, Cr, Al, Si)-oxide scale. SEM/EDX-analysis showed that the average composition of the inward-growing oxide scale was about 50 at% Fe, 20 at% Cr, 15 at % Al and 10 at% Si. However, Cr-enrichment was observed close to the metal oxide interface, displaying Cr-contents of up to 50 at% (SEM-EDX). Similar Cr-enrichment could be observed in the areas with a thinner oxide scale but not in the areas with thicker oxide scale. The areas with higher oxide thickness displayed highly porous outward-growing Fe oxide, mixed with traces of unreacted KCl. Less variation in oxide thickness was observed upon analyzing the Fe**10Cr**AlSi alloy after 168 h of exposure in the tube furnace (10–23 μm). Fig. 6b displays one of the thicker oxide scales, consisting of a 13 μm thick outward-growing Fe oxide scale and an 8 μm thick inward growing (Fe, Cr, Al, Si)-oxide scale. No distinct differences in contrast can be observed in the outward growing Fe oxide. However, the presence of both hematite (outer part) and magnetite (inner part) was identified with EBSD analysis as shown in the EBSD patterns inserted in Fig. 6. In addition, the EBSD analysis identified the inward-growing oxide as spinel. SEM/EDX analysis showed that the average composition of the spinel oxide is 50 at % Fe, 20 at% Cr, 15 at% Al and 10 at% Si. However, a 1–2 μm thick layer, enriched in Cr (56 at%) and depleted in Fe (20 at%) was detected with SEM-EDX in the inward-growing scale, close to the metal/oxide interface. Similar Cr-enrichment was observed in regions with thinner oxide scales. Both after 48 h and 168 h of exposure, a nitridation zone of 4–5 μm and 10–15 μm in thickness, respectively, was observed beneath the oxide scale. SEM-EDX analysis indicated the presence of Al-nitrides.

3.3.3. Alloy Fe15CrAlSi (KCl)

Fig. 7 shows SEM-BSE cross section images of the Fe**15Cr**AlSi alloy after exposure in the thermobalance for 48 h (Fig. 7a) and the tube furnace for 168 h (Fig. 7b). The Fe**15Cr**AlSi alloy formed a 5–14 μm thick oxide scale (with an average of around 6 μm) after 48 h of exposure in the thermobalance,. The general microstructure of the oxide scale is similar to those displayed by Fe**5Cr**AlSi and Fe**10Cr**AlSi with about 60–70% outward-growing Fe oxide and 30–40% inward-growing (Fe, Cr, Al, Si)-oxide. After 168 h of exposure in the tube furnace, the Fe**15Cr**AlSi alloy had formed an oxide scale with a similar microstructure as after 48 h of exposure but with an increased average oxide thickness (about 10 μm). No distinct differences in contrast were observed in the outward-growing Fe oxide but both hematite and magnetite were identified with XRD and EBSD analysis, respectively (not shown). The contrast in the SEM/BSE images of the inward-growing oxide scale is relatively even, indicating a uniform element distribution and density. However, close to the metal/oxide interface, the contrast is slightly brighter. Beneath the oxide scale, a 5–10 μm thick nitridation zone was observed after both 48 and 168 h of exposure. Both the SEM/EDX and STEM/EDX (see below) analysis showed enrichment of Al in this area compared to the alloy, indicating the formation of Al nitrides.

In areas with large amounts of former KCl particles, K_2CrO_4 was observed. At some of these areas grain boundary attack could be observed (see Fig. 7a), reaching depths of about 25 μm. SEM-EDX analysis indicated that while the majority of the attacked grain boundaries were enriched in Cr, the metal along attacked and non-attacked grain boundaries were depleted in Cr, see Fig. 8. In addition, indications of void formation were observed at the attacked grain boundaries deeper down in the alloy (Fig. 8a). Additionally, traces of Cl were detected in the attacked grain boundaries with SEM-EDX.

In order to investigate the microstructure of the slower growing oxide scale of the Fe**15Cr**AlSi alloy a detailed microstructural investigation was performed on one of the samples exposed for 48 h. A FIB lamella was lifted out from a representative region in the BIB cross-section with the FIB/SEM instrument (see Fig. 7). Fig. 9a shows a

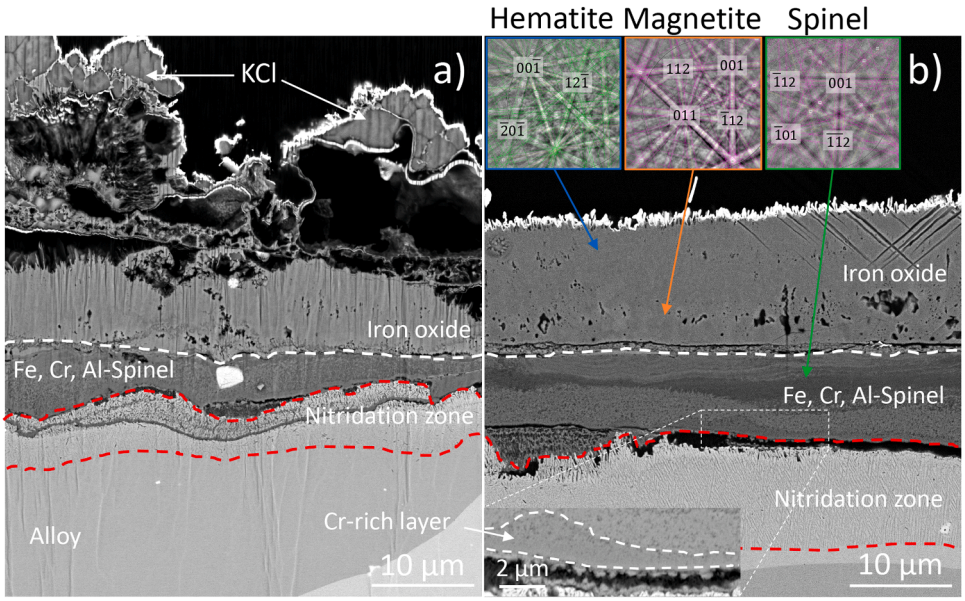

Fig. 6. SEM-BSE cross section images of Fe**10Cr**AlSi after being exposed to 5% O_2 + 20% H_2O at 600 °C with KCl present in a) a thermobalance for 48 h and b) a tube furnace for 168 h. The EBSD patterns in the blue, orange and green boxes (from left to right) confirms the presence of hematite, magnetite and spinel respectively. (For interpretation of the references to colour in this figure legend, the reader is referred to the web version of this article.)

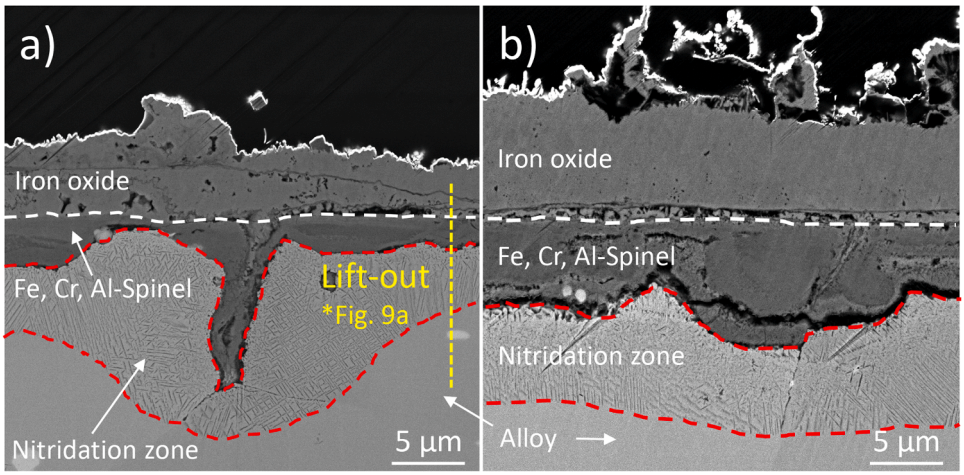

Fig. 7. SEM-BSE cross section images of Fe**15Cr**AlSi after being exposed to 5% O_2 + 20% H_2O at 600 °C with KCl present in a) a thermobalance for 48 h and b) a tube furnace for 168 h. *The yellow dashed line in Fig. 7a illustrates the area of the lift-out shown in Fig. 9a.

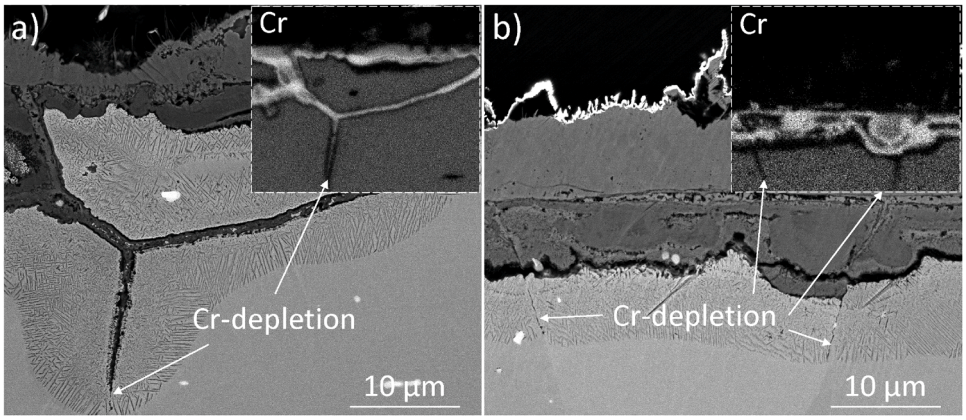

Fig. 8. SEM-BSE cross section images of Fe**15Cr**AlSi after being exposed to 5% O_2 + 20% H_2O at 600 °C with KCl present in a) a thermobalance for 48 h and b) a tube furnace for 168 h. SEM-EDX Cr maps of the respective areas are shown in the top right corner of Fig. 8a and Fig. 8b.

STEM high-angle annular dark field (HAADF) overview image of the Fe**15Cr**AlSi microstructure.

The oxide scale can be divided into three main layers (see Fig. 9a). The outer most layer was characterized as Fe oxide while two layers could be distinguished in the inward-growing scale, i.e., a dark and bright layer, in good agreement with the SEM investigation. A nitridation zone was observed beneath the oxide scale. In-between the outward growing Fe oxide and the inward growing scale a complex microstructure could be observed. This was interpreted as remains from the primary scale and chromate formation.

Fig. 9c shows a STEM-EDX line scan profile performed on a representative region marked with an arrow in Fig. 9a, illustrating the distribution of different elements within these layers. The different layers were in addition characterized with point analysis and electron diffraction (see Fig. 9b). From the line scan profiles, the top layer was identified as Fe oxide while the region at the original metal oxide interface had a very complex microstructure, i.e., increased Si/K/Cr content.

The first part of the inward growing scale (layer I) had a microstructure interpreted as less dense (darker contrast in the HAADF image) than the bottom part and had a composition of approximately 40 at% Cr, 10 at% Al and 35 at% Fe, 10 at% Si and 1 at% K. There were also indications of small amounts of Cl (less than 1 at%) in this region.

The bottom part (layer II), i.e., closest to the nitridation zone, had a different type of microstructure (interpreted as denser due to the brighter HAADF contrast) and a composition of approximately 65–70 at % Cr, 10 at% Al and 10–15 at% Fe, 5 at% Si. None or very low amounts of K/Cl were detected in this layer. A depletion zone of Cr was found below the oxide scale to a depth of approximately 400 nm.

The crystal structure of the inward-growing scale was investigated with convergent beam electron diffraction (CBED), see Fig. 9b. Both layers contain crystalline phases, and the presence of spinel structure was identified in both layers with the zone axis [1 1 2] (see inserts in Fig. 9b). However, the presence of a spinel phase in a region with a large amount of Cr/Al (dense bottom layer) indicate a more complex microstructure consisting of several phases. Additionally, the TEM lamella was thicker in this region and further detailed investigations are required to fully reveal the complex microstructure.

3.3.4. *Alloy Fe20CrAlSi (KCl)*

Fig. 10 shows SEM-BSE cross section images of the Fe**20Cr**AlSi alloy after exposure in a thermobalance for 48 h (Fig. 10a) and a tube furnace for 168 h (Fig. 10b). The Fe**20Cr**AlSi alloy formed equally thick oxide after 48 h and 168 h of exposure and is in the range 1–4 µm. The oxide scale consists of an approximately 1–3 µm thick outward growing Fe oxide and a 0.5–1 µm thick inward-growing oxide scale, distinguished by a darker contrast (see high magnification image in bottom left corner of Fig. 10b).

The Fe oxide is mixed with overgrown K_2CrO_4 giving a complex microstructure. Beneath the oxide scale, a nitridation zone could be

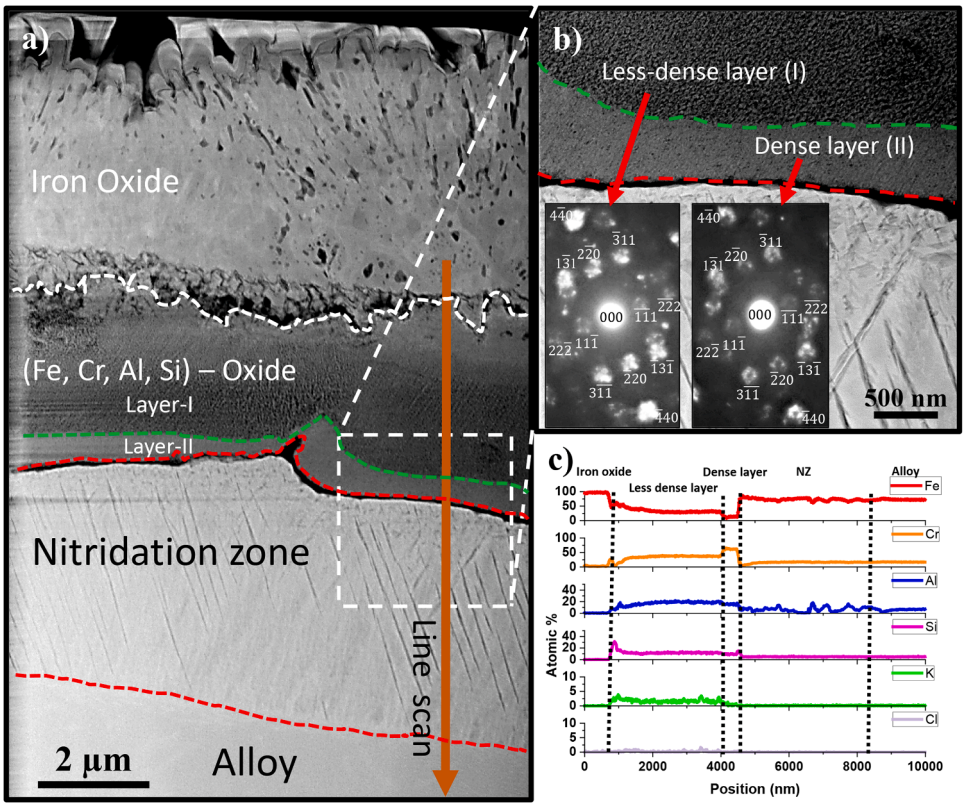

Fig. 9. a) STEM-HAADF image from a lift-out performed on Fe**15Cr**AlSi after being exposed to 5% O_2 + 20% H_2O at 600 °C with KCl present in a thermobalance in for 48 h. Fig. 9b shows a higher magnification STEM-HAADF image of the area marked in Fig. 9a with CBED patterns of the two different layers within the inward-growing scale. Fig. 9c displays the EDX-data corresponding to the line scan marked out in Fig. 9*a*.

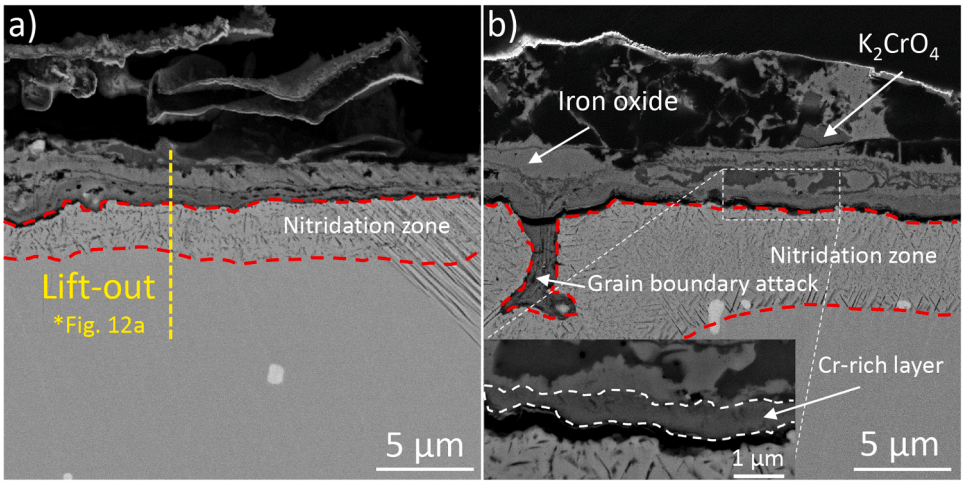

Fig. 10. SEM-BSE cross section images of Fe**20Cr**AlSi after being exposed to 5% O_2 + 20% H_2O at 600 °C with KCl present in a) a thermobalance for 48 h and b) a tube furnace for 168 h. *The yellow dashed line in Fig. 10a illustrates the area of the lift-out shown in Fig. 12a. (For interpretation of the references to colour in this figure legend, the reader is referred to the web version of this article.)

observed after both 48 and 168 h of exposure (to a depth of 1–3 µm and 5–10 µm respectively). Both the SEM/EDX and STEM/EDX analysis (see below) showed enrichment of Al in this area compared to the alloy, indicating Al nitrides. K_2CrO_4 was found in areas with large amounts of former KCl particles. Similar to the Fe**15Cr**AlSi alloy, grain boundary attack was also observed for Fe**20Cr**AlSi but to a higher degree, as shown in Fig. 11.

A detailed microstructural investigation (TEM) was performed on the Fe**20Cr**AlSi alloy after exposure for 48 h. A FIB lamella was lifted out from a representative region in the BIB cross-section (see Fig. 10a). Fig. 12a shows a STEM high-angle annular dark field (HAADF) overview image of the corrosion products. The corrosion products may be divided into several layers. The outer part consists of Cr/K and was interpreted as potassium chromate. Beneath that, a complex layer, consisting of dark and bright contrast regions, was found. This was followed by an Fe oxide layer. Below the Fe oxide layer, a Cr-rich scale (interpreted as the inward-growing scale) was found. The microstructure and composition of this scale are complex and small brighter regions could be observed

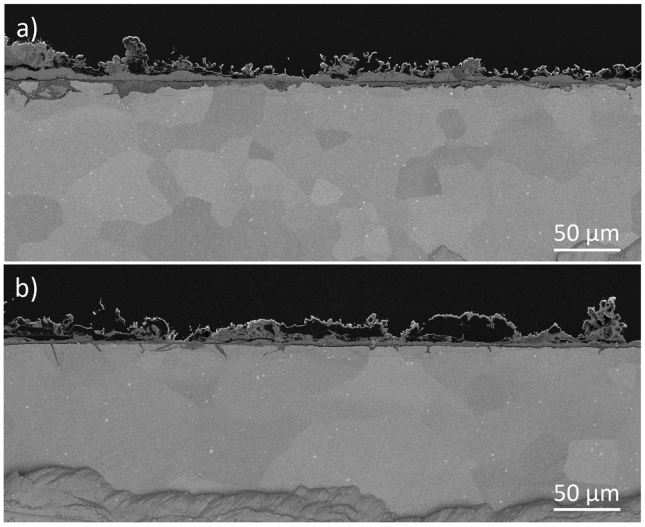

Fig. 11. SEM-BSE cross section images of a) Fe**15Cr**AlSi and b) Fe**20Cr**AlSi after being exposed to 5% O_2 + *20% H_2O* at 600 °C with KCl present for 168 h in a tube furnace.

throughout the layer in the STEM-HAADF image (Fig. 12a). It may be noted that none or very small amounts of Fe was found in this layer.

The different layers were in addition characterized with point analysis and electron diffraction. From STEM-EDX quantification analysis and line scan profile (see Fig. 12c) the compositions of the different layers were determined. Following the K_2CrO_4, Si-rich dark contrast regions (80 at% Si) and an Fe-rich (75 at% Fe) layer with about 7 at% Al and 8 at% Cr was found with indications of small amounts of K and Cl. This was followed by an outward-growing (interpreted) Fe oxide. The inward growing scale had an inhomogeneous elemental distribution across the layer (75–100 at% Cr, 0–10 at% Al and 0–20 at% Fe, 0–5 at% Si). A depletion zone of Cr was detected below the oxide scale to a depth of approximately 500 nm. The dark bands in the nitridation zone were quantified to be Al rich, indicating Al-nitrides.

The crystal structure of the inward-growing scale was investigated with CBED, see Fig. 12b. All layers contained crystalline phases. The presence of spinel structure was identified with the zone axis [0 0 1] in the marked layer, see insert in Fig. 12b. However, the presence of the spinel phase in a region with a large amount of Cr/Al indicate a more complex microstructure consisting of several phases. This is supported by the un-even contrast of the HAADF image with bright regions in this layer. In addition, the TEM lamella is thicker in this region and further detailed investigations are required to fully reveal the complex microstructure.

4. Discussion

The oxidation kinetics have been shown to be fundamentally different for Fe based alloys at 600 °C before and after breakaway corrosion (primary and secondary corrosion regimes respectively) [11]. The discussion is therefore separated into a primary part (before breakaway) and the secondary part (after breakaway). However, as the main aim of this study is to investigate the effect of Cr on the corrosion behavior of FeCrAl-Si model alloys in harsh environments, i.e., in which the alloys transition into the secondary corrosion regime, more emphasis is put on the exposures of FeCrAl model alloys in the presence of water vapor and KCl.

4.1. The primary protection

All model alloys managed to retain the primary protection (thin slow-growing oxide scale) during exposure in the presence of water vapor (and absence of KCl), see Fig. 1 and Fig. 3. This may be expected

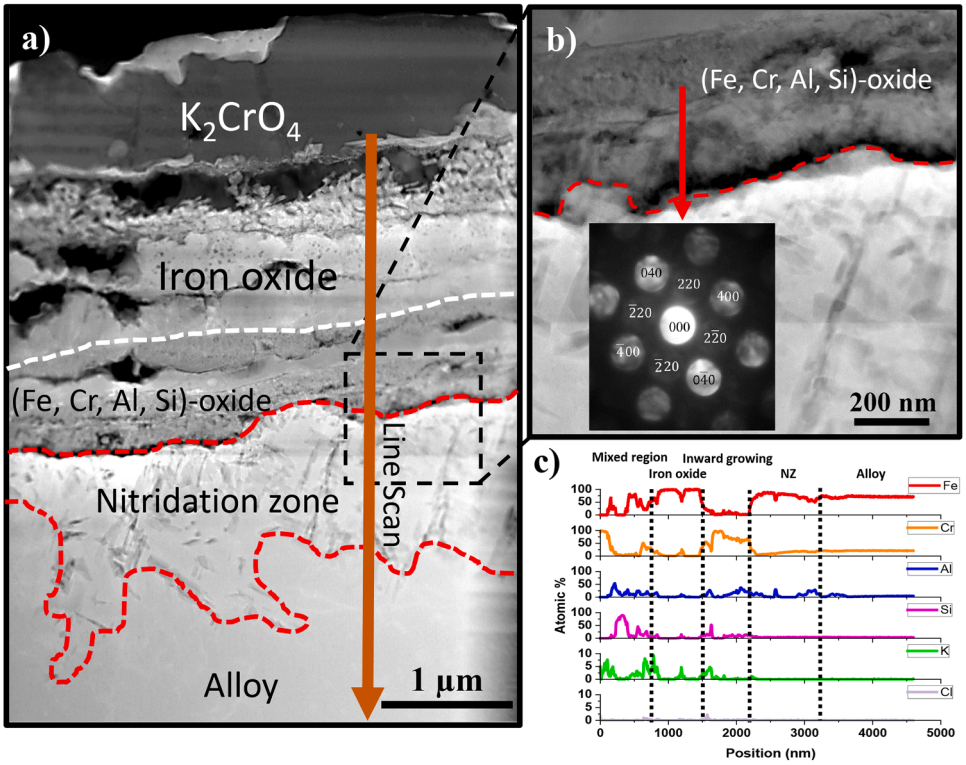

Fig. 12. a) STEM-HAADF image from a lift-out performed on Fe**15Cr**AlSi after being exposed in a thermobalance at 600 °C in 5% O_2 + 20% H_2O with KCl present for 48 h. Fig. 12b shows a higher magnification STEM-HAADF image of the area marked in Fig. 12a with CBED pattern of the marked layer within the inward-growing scale. Fig. 12c displays the EDX-data corresponding to the line scan marked out in Fig. 12a.

for the alloys with high Cr contents since they have a greater reservoir of Cr that may compensate for the Cr-evaporation from the Al/Cr-rich protective oxide scale. However, in this study, two alloys with relatively low amounts of Cr, Fe**5Cr**AlSi and Fe**10Cr**AlSi, were also able to retain the primary protection. This may be compared to FeCr model alloys where alloys with a Cr-content of up to 25% lost their primary protection in the presence of water vapor at 600 °C [23]. In addition, Lim et al. showed that FeCrAl alloys should contain at least 4–5 wt% Al and 10–12 wt% Cr in order to form a protective layer at 600 °C [24]. Both Fe**5Cr**AlSi and Fe**10Cr**AlSi are below the optimal range (especially the former) but still forms protective oxide scales.

The influence of Si on the primary protection of lean FeCrAl alloys (low Cr-content) at 600 °C was recently studied [14]. The study showed that minor additions of Si significantly improve the primary protection of these alloys by preventing breakaway oxidation in the presence of water vapor. This was further investigated in a study by Asokan et al. which showed that the addition of Si to FeCrAl model alloys results in the formation of a primary oxide scale with higher concentration of Al when exposed under dry conditions [25]. The experimental findings were in agreement with thermodynamic calculations, indicating increased Al-activity and reduced Cr-activity in the alloy in the presence of Si. Additionally, the Si-containing FeCrAl alloy was shown to form a protective oxide scale, highly enriched in Si and Al with only traces of Cr when exposed under wet conditions which may further explain the resistance towards water vapor.

Sparsely distributed Fe oxide nodules, seemingly originating at reactive element particles, were found on the surface of the Fe**5Cr**AlSi alloy. This phenomenon has been observed in previous studies [14,26–28]. Boggs et al. reported Fe oxide nodules on binary Fe-Al alloys and proposed that they form due to localized breakdown of the protective alumina under which the adjacent metal was depleted in Al [26]. However, Tomaszewicz et al. claim that the Fe oxide nodules form in the initial stages of oxidation and that a healing layer may form since the nodules do not grow or increase in number during further oxidation [27]. This is in good agreement with the work by Zhang et al. which showed demonstrated similar self-healing behavior and indicated a high enrichment of Al at the oxide/metal interface underneath the Fe oxide nodules [28]. Nevertheless, all model alloys in the present study displayed a protective behavior on the majority of the sample surfaces, i.e., all FeCrAl model alloys remained in the primary corrosion regime and the Fe rich nodules did not function as initiation points for breakaway oxidation.

4.2. The secondary protection – behavior after breakaway oxidation

4.2.1. Initiation

All alloys went into breakaway oxidation in the presence of KCl, see Figs. 1, 2 and 4. This is in good agreement with earlier studies of FeCrAl alloys exposed in harsh environments, especially at lower temperatures at which α-alumina formation is slow [12,29,30].

Alkali- and chlorine-containing species have been shown to break down the primary scale through various mechanisms, such as Cr depletion due to formation of K_2CrO_4 (alkali compounds) [6,9,31,32] or chlorine-induced corrosion [33–35]. This usually results in rapid formation of Fe-rich oxide which, because of the higher growth rate compared to chromia and alumina, is considered less protective [12,14,29,30]. A common perception is that increasing the Cr content in chromia-forming steels, exposed in an environment containing water vapor or other Cr-depleting species, increases the incubation time of the alloy, i.e., the time before the chromia breaks down. This was shown by Pujilaksono et al. when exposing several FeCr model alloys with varying Cr content in a water vapor containing environment [23]. However, the results of the present study show that the transition from the primary to the secondary regime occurs immediately (revealed by the initially high mass gain recorded in the thermo balance) for all alloys, i.e., none of the alloys displayed a significant incubation time. It should be noted that the formation of K_2CrO_4 may be partly responsible for the initial mass gain while the microstructure supports the conclusion of a very rapid transition to the secondary regime. The calculated α-values (Table 2) indicate that the initial oxide scale on all alloys except for the Fe**5Cr**AlSi alloy grow parabolically. The low initial α-value (<1) of the Fe**5Cr**AlSi alloy indicates exponential growth while the other alloys show partially parabolic behavior. As several processes possibly influencing the mass change may be at play simultaneously (oxidation, evaporation (KCl), K_2CrO_4 formation) it is challenging to draw more conclusions during the very initial stages based on the calculated α-values.

4.2.2. Propagation

The mass gain data shows that increasing the Cr content has a large influence on the kinetics of the corrosion process after the transition from the primary to the secondary corrosion regime, displaying drastically reduced corrosion rates with elevated Cr content, see Figs. 1–2. This is in agreement with a previous study, investigating the corrosion behavior of FeCrAl model alloys (without Si) within the secondary corrosion regime (using K_2CO_3 instead of KCl) [11]. However, it may be noted that the corrosion rate only decreased when exceeding a Cr-content of 18 wt% without additions of Si, i.e., with a Cr concentration below 18 wt% the Cr-content had no influence on the corrosion behavior in the secondary regime. In contrast, the Cr-content significantly influenced the oxidation kinetics even at 10 wt% in the present study, i.e., FeCrAl alloys containing Si.

The calculated α-values, shown in Table 2, provide some additional insight in the propagation of the corrosion behavior of the different alloys. After the initial exponential behavior (α<1) of the Fe**5Cr**AlSi alloy during the first two hours of the exposure, it displayed an abrupt transition into a sub-parabolic behavior (α=5). This transition is indicative of the sample surface reaching full coverage of the rapidly growing Fe-rich oxide scale within the first two hours and that propagation from that point is limited by the diffusion of ions through the thick oxide scale. However, it may be noted that a Fe10Cr4Al model alloy (without Si) exhibited a significantly higher mass gain and did not transition into sub-parabolic behavior when exposed under the same exposure conditions [36], indicating that other mechanisms, related to the presence of Si in the alloy, may be in play. While the Fe**5Cr**AlSi and Fe**10Cr**AlSi alloys exhibited similar mass gain after 48 h of exposure, the former displayed rapid initial oxidation followed by an early transition into sub-parabolic behavior and the latter displayed a slower initial oxidation rate but transition into sub-parabolic behavior at a later stage. Meanwhile, the Fe**5Cr**AlSi and Fe**10Cr**AlSi alloys displayed large differences in mass gain after 168 h of exposure. In addition, the mass gain of the latter was twice as high after 48 h than after 168 h of exposure. This discrepancy may be connected to the difference in flow rate in the two systems (3 cm/s in the tube furnace and 1.5 cm/s in the thermobalance), which was shown to significantly affect the evaporation rate of KCl (0.03 mg/cm^2 h in tube furnace and 0.008 mg/cm^2 h in the thermobalance). Thus, KCl(s) remained on the surface of the samples for a much longer time when exposed in the thermobalance in comparison to the tube furnace. Considering this, the mechanism responsible for the transition into sub-parabolic behavior may be suppressed by the longer exposure to KCl in the thermobalance.

The Fe**15Cr**AlSi and Fe**20Cr**AlSi alloy displayed initial parabolic kinetics followed by a transition into sub-parabolic behavior after 10 and 0.5 h respectively, indicating the formation of a healing layer. Accordingly, both alloys displayed similar mass gain after 48 and 168 h of exposure if taking the evaporation of KCl into account. This indicates that the longer exposure to KCl(s) in the thermobalance did not inhibit the transition into sub-parabolic behavior for the Fe**15Cr**AlSi and Fe**20Cr**AlSi alloys.

The oxide scale microstructure of Fe-based steels after transition into the secondary regime (after breakaway oxidation) has been abundantly reported to consist of outward-growing Fe oxide and inward-growing spinel (containing the main alloying elements) [11,20–23,29,37]. This

type of distribution of alloying elements has been attributed to the difference in diffusivities of the alloying elements in the spinel phase. Fe has a several orders of magnitude higher diffusivity than Cr and Al [11, 38–40]. Accordingly, all alloys investigated in this study display similar oxide scale microstructure (30–40% inward and 60–70% outward) within the secondary regime, see Figs. 5–10. However, the oxide scale thickness was greatly reduced upon increasing the Cr-content, see Fig. 13.

The outward-growing Fe oxide scale does not contain any (or a very low amount of) Cr, implying that Cr does not have a direct influence on the growth rate of this scale. In addition, nothing observed in the microstructure, i.e., grain size of hematite and magnetite layers, indicate that the outward growing scale is rate determining. Cr is instead present in the inward-growing oxide scale. The microstructural investigation shows that while the oxide scale thickness was reduced drastically with increasing Cr content, the ratio between inward- and outward-growing oxide scales remained approximately constant (40% inward and 60% outward). This suggests that the growth rates of these layers are connected. Since the Cr in the alloy, which seemingly has a large effect on the growth rate of the Fe-rich oxide scale, ends up in the inward-growing part, it is tempting to suggest that this layer is rate-determining for the oxidation process in the secondary corrosion regime.

It may be noted that no Si-rich layer was observed on any of the alloys and the formation of a protective silica layer may therefore be ruled out. Instead, higher concentration of Cr was detected close to the metal/oxide interface for both the Fe**10Cr**AlSi and Fe**15Cr**AlSi alloys and throughout the inward-growing scale of Fe**20**CrAlSi. There were no indications of this type of Cr-enrichment in the inward-growing scale of Fe**5Cr**AlSi. The transition into slow oxide scale growth may therefore be connected to the Cr-enrichment in the inward-growing scale.

Previous research often attributes these types of kinetic transitions to the formation of a corundum type healing layer [41–46], i.e., a Cr- and/or Al-rich corundum-type oxide scale that reforms at the metal/-oxide interface at some point after breakaway oxidation has occurred. However, the thickness of these layers (0.5–2 μm) indicates a significantly higher growth rate than what is expected for a (primary) Cr-rich corundum type oxide scale at the present temperature. Jonsson et al. and Pujilaksono et al. [20,23] reported that chromia scales formed on Fe10–25Cr alloys when exposed in dry O_2 at 600 °C was in the range 50–70 nm after 24 h and in the range 70–90 nm after 168 h which indicates a significantly lower growth rate than the Cr-rich layers in the present study. In addition, the CBED patterns obtained from the inward-growing scales of the Fe**15Cr**AlSi and Fe**20**CrAlSi alloys show presence of a spinel crystal structure in these regions. However, this does not rule out the presence of corundum type oxide since several phases may be present simultaneously. An example of the mentioned behavior was identified by Col et al. when analyzing a 304 L sample, exposed in dry air at 850 °C for 312 h, with Raman mapping [46]. The inner part of the inward-growing scale displayed Cr-rich spinel co-existing with Cr-rich corundum type oxide, indicating an imminent phase transformation from the former to the latter. The initial formation of a meta-stable Cr-rich spinel and subsequent transformation into a corundum type oxide could explain the relatively high thickness of the Cr-rich layers. The detailed microstructural investigation showed that the Cr- and Al-content in the innermost part of the inward-growing scale of Fe**15Cr**AlSi and the entire inward-growing scale of Fe**20**CrAlSi was higher than 67.7 at%, see Figs. 8 and 12. Since Cr and Al have been shown to be more restricted to be trivalent (maximum of 67.7 at% in the spinel crystal structure), the high concentration of Cr and Al provides a strong driving force to transform into corundum type oxide [47,48].

In the present work, 400–500 nm depletion zones (Cr) were observed below the slow-growing Cr-rich scales of Fe**15Cr**AlSi and Fe**20**CrAlSi, see Figs. 9 and 12. This indicates that the oxidation kinetics are slow and that the Cr-rich scales have been supplied with Cr from the alloy. Using diffusivity data from binary Fe–Cr alloys [49], measured at higher temperatures and extrapolated to 600 °C by Young et al. [50] (Using D_{Cr} of $10^{-14.5}$ cm^2 s^{-1}), a depletion zone of about 40 nm could be expected after 1 h exposure at 600 °C. Jonsson et al. found that the actual depth of the depletion zone of a Fe10Cr model alloy was about 80 nm after 1 h exposure at 600 °C, i.e. slightly higher than the estimated value [20]. Nevertheless, the significantly higher depth of the depletion zones found in this study, indicates that the depletion, and thereby the stabilization of the oxidation process, started at an early stage of the exposure and not during the final hours. This is in good agreement with TGA results which showed a transition into sub-parabolic behavior already during the first hours of exposure. This further supports that the Cr-enrichment in the inward-growing scale is connected to the stabilization of the oxidation process.

The corrosion resistance of the Cr-rich spinel and/or a possible transition into corundum type oxide in the initial part of the exposure is not fully understood. The significantly lower oxidation rate for the Fe**15Cr**AlSi and Fe**20Cr**AlSi during the first hours of exposure may be connected to the suppression of internal oxidation (equilibrium composition of the spinel mixed with Cr-depleted metal (BCC)). The formation of an internal oxidation zone has previously been connected to the formation of a porous inward-growing oxide scale, resulting in rapid oxidation within the secondary corrosion regime [11,20–22,46, 51–53]. This is in good agreement with the present study, which showed that none of the alloys that formed slow-growing oxide scales displayed internal oxidation. Eklund et al. [16] previously showed a connection between the formation of slow-growing oxide scales and the ability of an alloy to prevent internal oxidation. Detailed microstructural analysis revealed significant Cr-enrichment in the inward-growing part of the slow-growing oxide scales for which the obtained CBED patterns revealed the presence of both spinel and corundum type oxide, indicating the formation of a healing layer. Thermodynamic calculations in that work suggested that a Fe-Cr-(Al)-O system transition from the two-phase region BCC+S (internal oxidation zone) to a phase region, in which spinel is in equilibrium with corundum (S+C), when exceeding a critical Cr content. In addition, the incorporation of Al in the system was shown to reduce the stability of the internal oxidation zone, thereby reducing the critical Cr content necessary to prevent internal oxidation and enable the formation of a healing layer.

In the present study, all alloys displayed an Al concentration of about 15 at% in the inward growing scale and the corresponding phase diagram is shown in Fig. 14. The lines (solid and dashed) in Fig. 14 illustrate the range of Cr concentration (cationic%) that was detected in the inward growing scale of the four alloys. Among these alloys, only the

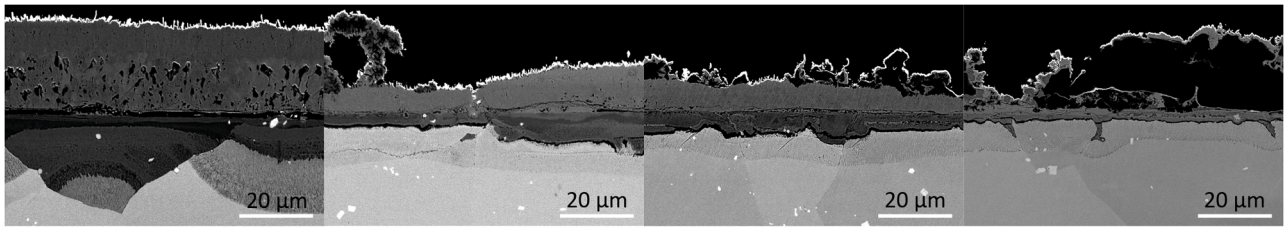

Fig. 13. SEM-BSE cross section images of a) Fe**5Cr**AlSi, b) Fe**10Cr**AlSi, c) Fe**15Cr**AlSi, and d) Fe**20Cr**AlSi after being exposed to 5% O_2 + 20% H_2O at 600 °C with KCl present for 168 h in a tube furnace.

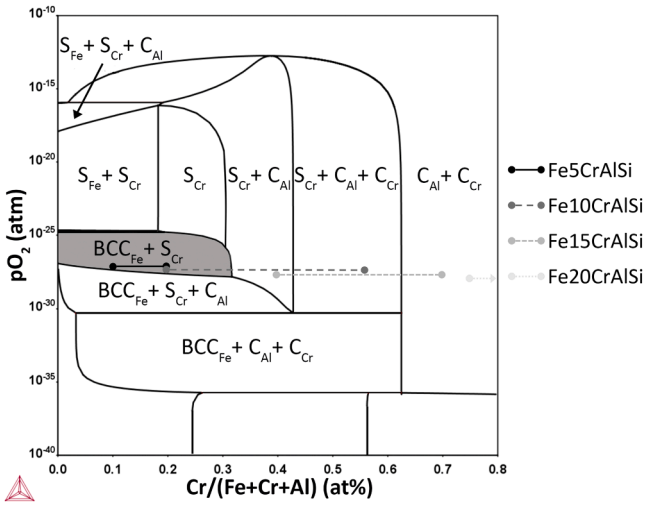

Fig. 14. Phase diagram for the FeCrAl-O system at 600 °C and Al concentration fixed at 15 at%, calculated with Thermo-Calc using the TCOX10 database. The subscripts of the different phases indicate if they are rich in Fe, Cr or Al. The two-phase region $BCC_{Fe}+S_{Cr}$, (internal oxidation zone) is highlighted in grey. The vertical lines indicate the range of Cr-content in the inward-growing scale, i.e., close to the metal/oxide interface (low pO_2), for the different alloys.

Fe5CrAlSi alloy has a Cr concentration range that is solely within the $BCC_{Fe}+S_{Cr}$ (internal oxidation zone) region. This agrees with the microstructural investigation which showed that only Fe5CrAlSi formed an internal oxidation zone. While the lower end of the Cr concentration range of Fe10CrAlSi is within the $BCC_{Fe}+S_{Cr}$ region, the upper end is within the S+C region. This could explain why the transition into sub-parabolic oxidation kinetics is suppressed for Fe10CrAlSi in the presence of higher amounts of KCl. Meanwhile, both Fe15CrAlSi and Fe20CrAlSi display Cr concentrations that are outside the $BCC_{Fe}+S_{Cr}$ region, which may explain their rapid transition into sub-parabolic behavior and the formation of a healing layer.

Since the present study indicates that the addition of Si further reduces the critical Cr content, incorporating Si in the Fe-Cr-Al-O system may influence the stability of the internal oxidation zone similar to adding Al to the Fe-Cr-O system. According to the microstructural investigation, the distribution of Si is relatively uniform in the inward-growing scale of all alloys. This indicates that Si has not precipitated in the form of dispersed SiO_2 particles or enriched in the grain boundaries but may instead be a part of the spinel crystal structure.

There are a few examples of Si-containing spinels, e.g., ringwoodite and the silicon-aluminum spinel [54,55]. However, these phases generally form at very high pressures and temperatures. Because of the relatively short exposures in the present study, the FeCrAlSi-O system have most likely not reached equilibrium and the distribution of elements may therefore deviate from the thermodynamically stable equilibrium. A possible microstructural evolution may be the formation of SiO2 regions in combination with a Si-free spinel after longer exposure times and reaching equilibrium. After discussion with the TCOX database developers it was decided that adding the Si-containing spinels to the database in ambient pressure and temperature is not physically correct and may only interfere with well-established systems. For this reason, the phase diagram calculated from Thermo-Calc using the TCOX10 database cannot be used to interpret this system which is why the phase diagram (in Fig. 14) was calculated without Si.

Nevertheless, in Si-containing spinels, Si tends to occupy tetrahedral sites. Since Si is tetravalent (Si^{4+}) and the tetrahedral sites are generally occupied by divalent ions, every Si^{4+} ion should induce one tetrahedral vacancy to maintain charge neutrality, see Fig. 15. In theory, this would mean that incorporating Si in the crystal structure would reduce the total number of ions in relation to a spinel without Si. Meanwhile, the number of Cr and Al ions would remain constant as these generally occupy the octahedral sites, resulting in increased atomic concentration of Cr and Al. If so, studying the phase diagrams in Fig. 14, makes it apparent that the incorporation of Si should facilitate the transition from the BCC + S (internal oxidation zone) phase region to the S + C (spinel and corundum in equilibrium) phase region and enable the formation of a healing layer at lower Cr content (in the alloy).

Alloy grain boundary attack was observed for both Fe**15Cr**AlSi and Fe**20Cr**AlSi (see Figs. 7–8 and 10–11), while no grain boundary attack was detected for the alloys with lower Cr content. A similar phenomenon was observed in another study in which FeCrAlSi model alloys were exposed in a waste-fired boiler [15]. It was shown that the general corrosion behavior improved with higher Cr content (reduced material loss) but that the acceleration of the corrosion attack was more prominent on the windward side (in the direction of the flue gas) for alloys with higher Cr-content. This was attributed to the direct contact with higher amounts of alkali chlorides and their interaction with Cr. The vital role of Cl on this phenomenon is strengthened by a previous study, in which FeCr(Al) alloys with elevated Cr-content did not display grain boundary attack after the primary protection was broken down with K_2CO_3, i.e. in the absence of Cl-ions [11].

The mechanism behind grain boundary attack in the presence of Cl-containing species has previously been investigated [56–59]. Malede et al. showed correlations between the formation of Cr-rich σ-phase along the grain boundaries and subsequent selective attack of these in the presence of KCl. This was attributed to interaction between Cl-ions and the Cr-rich σ-phase, resulting in the formation of volatile

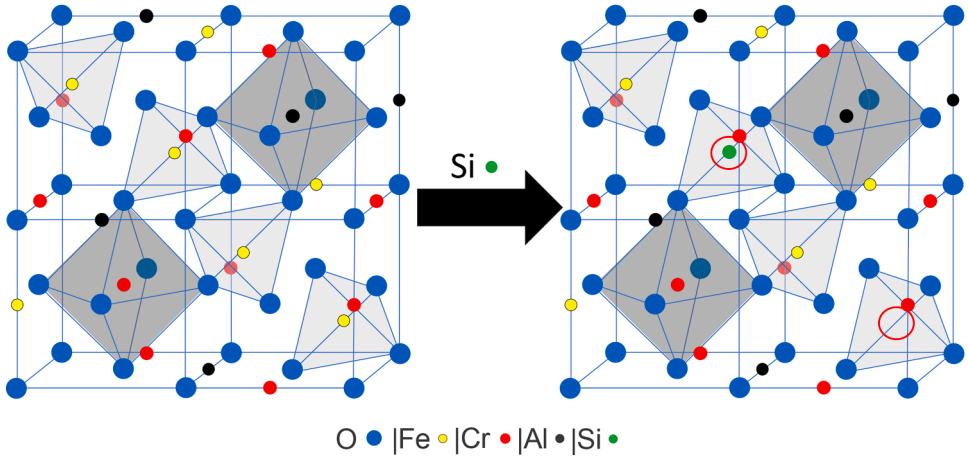

Fig. 15. Schematic illustration of the induction of vacancies in the tetrahedral sites upon incorporation of Si into the spinel crystal structure.

Cr-chlorides, $CrCl_2$, followed by depletion of Cr along the grain boundaries and consequently, reduced corrosion resistance. While the formation of σ-phase is more rapid in the presence of ferrite stabilizers [60] such as Cr and Si, it is very slow at 600 °C [61–64] and may not be a viable explanation for the observations in the present study. Jonsson et al. suggested an alternative mechanism, involving the preferential attack of the grain boundaries in the presence of HCl. This was attributed to the formation of voids along the grain boundaries because of rapid outward flux of Cr and Fe and that metal chlorides preferentially form along these voids [58]. In addition, the formation of metal chlorides is suggested to further accelerate the void formation because of the high ionic conduction of these. This agrees with the observations of the present study, which clearly displays Cr-depletion along attacked and non-attacked grain boundaries as well as indications of void formation. Traces of Cl in the attacked grain boundaries further supports this mechanism.

5. Conclusions

The main aim of the present paper was to investigate the influence of Cr-content on the oxidation behavior of Si-containing FeCrAl alloys after breakaway oxidation (secondary protection). Deposition of KCl salt was utilized to ensure rapid transition into the secondary corrosion regime (trigger breakaway oxidation). This was successful for all the alloys investigated in the present study, resulting in the formation of an Fe-rich oxide scale.

By increasing the Cr content in the model alloys, the oxidation behavior after breakaway oxidation was altered, transitioning from parabolic to sub-parabolic oxide growth which significantly reduced the oxide scale thickness. This kinetic transition occurred at an earlier stage with increasing Cr-content and was attributed to the formation of a Cr-rich healing layer. It is suggested that the formation of a healing layer was enabled by preventing internal oxidation which according to thermodynamic calculations is inhibited by the enrichment of Cr in the inward-growing scale.

However, in addition to the positive influence of Cr, elevated Cr-content (≥15 wt% Cr) in the alloy made the alloy more prone to alloy grain boundary attack which may negatively affect the longevity of the material during long-term operation.

Although the behavior after breakaway oxidation was the main focus of the present study, the reference exposures (in the absence of KCl) provided some insight into the influence of Si within the primary corrosion regime. Since all alloys, with Cr-contents ranging from 5 to 20 wt%, formed and retained a thin protective oxide scale in the presence of oxygen and water vapor, the results indicate that Si may reduce the minimum Cr- and Al-content necessary to form a protective layer.

CRediT authorship contribution statement

Johan Eklund: Conceptualization, Methodology, Validation, Investigation, Data curation, Writing – original draft, Writing – review & editing, Visualization. **Imran Hanif:** Investigation, Writing – review & editing. **Sedigheh Bigdeli:** Software, Writing – review & editing., **Torbjörn Jonsson:** Conceptualization, Writing – review & Editing, Supervision, Project administration, Funding acquisition.

Declaration of Competing Interest

The authors declare that they have no known competing financial interests or personal relationships that could have appeared to influence the work reported in this paper.

Data availability

The raw/processed data required to reproduce these findings cannot be shared at this time due to technical or time limitations.

Acknowledgements

This work was carried out within the High Temperature Corrosion Centre (HTC) at Chalmers University of Technology and with support from the Swedish Energy Agency and the member companies (AB Sandvik Materials Technology, Kanthal AB, Energiforsk AB, MH Engineering AB, Thermo-Cale Software AB, Valmet Technologies Oy, Sumitumo SHI FW Energia Oy, Babcock and Wilcox Volund A/S and MEC BioHeat and Power A/S). The research was performed in part at the Chalmers Materials Analysis Laboratory, CMAL.

References

[1] P. Kofstad, HigH Temperature Corrosion, Elsevier applied science, London; New York, N.Y, 1988.
[2] H. Götlind, F. Liu, J.E. Svensson, M. Halvarsson, L.G. Johansson, The effect of water vapor on the initial stages of oxidation of the FeCrAl alloy kanthal AF at 900 °C, Oxid. Met. 67 (2007) 251–266.
[3] F. Liu, H. Josefsson, J.-E. Svensson, L.-G. Johansson, M. Halvarsson, TEM investigation of the oxide scales formed on a FeCrAlRE alloy (Kanthal AF) at 900°C in dry O2 and O2 with 40% H2O, Mater. High. Temp. 22 (2005) 521–526.
[4] D.J. Young, High Temperature, Oxidation and Corrosion of Metals, Elsevier, 2008.
[5] H. Asteman, K. Segerdahl, J.E. Svensson, L.G. Johansson, M. Halvarsson, J.E. Tang, p. trans tech, Oxidation of stainless steel in H2O/O-2 environments - Role of chromium evaporation, in: P. Steinmetz, I.G. Wright, G. Meier, A. Galerie, B. Pieraggi, R. Podor (Eds.), High Temperature Corrosion and Protection of Materials 6, Prt 1 and 2, Proceedings, Trans Tech Publications Ltd, Zurich-Uetikon, 2004, pp. 775–782.
[6] J. Pettersson, N. Folkeson, L.-G. Johansson, J.-E. Svensson, The Effects of KCl, K2SO4 and K2CO3 on the high temperature corrosion of a 304-type austenitic stainless steel, Oxid. Met. 76 (2011) 93–109.
[7] C. Pettersson, L.G. Johansson, J.E. Svensson, The influence of small amounts of KCl (s) on the initial stages of the corrosion of alloy sanicro 28 at 600 °C, Oxid. Met. 70 (2008) 241–256.
[8] S. Karlsson, J. Pettersson, L.G. Johansson, J.E. Svensson, Alkali induced high temperature corrosion of stainless steel: the influence of NaCl, KCl and CaCl2, Oxid. Met. 78 (2012) 83–102.
[9] Y.S. Li, Y. Niu, M. Spiegel, High temperature interaction of Al/Si-modified Fe–Cr alloys with KCl, Corros. Sci. 49 (2007) 1799–1815.
[10] J.X. Sui, J. Lehmusto, M. Bergelin, M. Hupa, The effects of KCl, NaCl and K2CO3 on the high-temperature oxidation onset of sanicro 28 steel, Oxid. Met 85 (2016) 565–598.
[11] A. Persdotter, J. Eklund, J. Liske, T. Jonsson, Beyond breakaway corrosion - influence of chromium, nickel and aluminium on corrosion of iron-based alloys at 600 °C, Corros. Sci. (2020), 108961.
[12] N. Israelsson, K. Hellström, J.-E. Svensson, L.-G. Johansson, KCl-induced corrosion of the FeCrAl alloy kanthal ® AF at 600 °C and the effect of H2O, Oxid. Met. 83 (2015) 1–27.
[13] H. Josefsson, F. Liu, J.E. Svensson, M. Halvarsson, L.G. Johansson, Oxidation of FeCrAl alloys at 500–900°C in dry O2, materials and corrosion 56 (2005) 801–805.
[14] J. Eklund, B. Jönsson, A. Persdotter, J. Liske, J. Svensson, T. Jonsson, The influence of silicon on the corrosion properties of FeCrAl model alloys in oxidizing environments at 600° C, Corros. Sci. (2018).
[15] J. Eklund, M.D. Paz, B. Jönsson, J. Liske, J.-E. Svensson, T. Jonsson, Field exposure of FeCrAl model alloys in a waste-fired boiler at 600°C: The influence of Cr and Si on the corrosion behaviour, 0.
[16] J. Eklund, A. Persdotter, I. Hanif, S. Bigdeli, T. Jonsson, Secondary corrosion protection of FeCr(Al) model alloys at 600 °C – The influence of Cr and Al after breakaway corrosion, Corros. Sci. 189 (2021), 109584.
[17] R.S. Bradley, P. Volans, Rates of Evaporation. VI. The Vapour Pressure and Rate of Evaporation of Potassium Chloride, Proceedings of the Royal Society of London. Series A, Mathematical and Physical Sciences, 217 (1953) 508–523.
[18] T. Sand, C. Geers, Y. Cao, J.E. Svensson, L.G. Johansson, Effective reduction of chromium-oxy-hydroxide evaporation from Ni-base alloy 690, Oxid. Met. 92 (2019) 259–279.
[19] J. Eklund, B. Jönsson, A. Persdotter, J. Liske, J.E. Svensson, T. Jonsson, The influence of silicon on the corrosion properties of FeCrAl model alloys in oxidizing environments at 600 °C, Corros. Sci. 144 (2018) 266–276.
[20] T. Jonsson, B. Pujilaksono, H. Heidari, F. Liu, J.E. Svensson, M. Halvarsson, L. G. Johansson, Oxidation of Fe–10Cr in O2 and in O2+H2O environment at 600°C: A microstructural investigation, Corros. Sci. 75 (2013) 326–336.
[21] T. Jonsson, H. Larsson, S. Karlsson, H. Hooshyar, M. Sattari, J. Liske, J.E. Svensson, L.G. Johansson, High-temperature oxidation of FeCr(Ni) alloys: the behaviour after breakaway, Oxid. Met. 87 (2017) 333–341.
[22] T. Jonsson, S. Karlsson, H. Hooshyar, M. Sattari, J. Liske, J.E. Svensson, L. G. Johansson, Oxidation after breakdown of the chromium-rich scale on stainless steels at high temperature: internal oxidation, Oxid. Met. 85 (2016) 509–536.
[23] B. Pujilaksono, T. Jonsson, H. Heidari, M. Halvarsson, J.E. Svensson, L. G. Johansson, Oxidation of binary FeCr alloys (Fe–2.25Cr, Fe–10Cr, Fe–18Cr and Fe–25Cr) in O2 and in O2 + H2O environment at 600 °C, Oxid. Met. 75 (2011) 183–207.

[24] J. Lim, I.S. Hwang, J.H. Kim, Design of alumina forming FeCrAl steels for lead or lead–bismuth cooled fast reactors, J. Nucl. Mater. 441 (2013) 650–660.
[25] V. Asokan, J. Eklund, S. Bigdeli, T. Jonsson, The influence of Si on the primary protection of lean FeCrAl model alloys in O2 and O2+H2O at 600 °C—A microstructural investigation, Corros. Sci. 179 (2021), 109155.
[26] W.E. Boggs, Oxid. Iron-Aluminum Alloy. 450° 900°C 118 (1971) 906–913.
[27] P. Tomaszewicz, G.R. Wallwork, Obs. nodule Growth Oxid. pure Bin. iron-Alum. Alloy. 19 (1983) 165–185.
[28] Z.G. Zhang, F. Gesmundo, P.Y. Hou, Y. Niu, Criteria for the formation of protective Al2O3 scales on Fe–Al and Fe–Cr–Al alloys, Corros. Sci. 48 (2006) 741–765.
[29] N. Israelsson, K.A. Unocic, K. Hellström, T. Jonsson, M. Norell, J.-E. Svensson, L.-G. Johansson, A. Microstructural, and kinetic investigation of the KCl-induced corrosion of an FeCrAl Alloy at 600 °C, Oxid. Met. 84 (2015) 105–127.
[30] N. Israelsson, High Temperature Oxidation and Chlorination of FeCrAl Alloys, in, Chalmers University of Technology, 2014.
[31] J. Pettersson, H. Asteman, J.E. Svensson, L.G. Johansson, KCl induced corrosion of a 304-type austenitic stainless steel at 600°C; the role of potassium, Oxid. Met. 64 (2005) 23–41.
[32] S. Karlsson, J. Pettersson, L.-G. Johansson, J.-E. Svensson, Alkali induced high temperature corrosion of stainless steel: the influence of NaCl, KCl and CaCl2, Oxid. Met. 78 (2012) 83–102.
[33] H.P. Nielsen, F.J. Frandsen, K. Dam-Johansen, L.L. Baxter, The implications of chlorine-associated corrosion on the operation of biomass-fired boilers, Prog. Energy Combust. Sci. 26 (2000) 283–298.
[34] A. Zahs, M. Spiegel, H.J. Grabke, The influence of alloying elements on the chlorine-induced high temperature corrosion of Fe-Cr alloys in oxidizing atmospheres, Mater. Corros. -Werkst. Und Korros. 50 (1999) 561–578.
[35] A. Zahs, M. Spiegel, H.J. Grabke, Chloridation and oxidation of iron, chromium, nickel and their alloys in chloridizing and oxidizing atmospheres at 400-700 degrees C, Corros. Sci. 42 (2000) 1093–1122.
[36] J. Eklund, Material Solutions for Mitigating High Temperature Corrosion in Biomass- and Waste-fired Boilers - Utilizing Novel FeCrAl Alloys and HVAF-sprayed Ni-based Coatings, in: The Department of Chemistry and Chemical Engineering, Chalmers University of Technology, 2018.
[37] T. Jonsson, Microscopy of high temperature oxidation of iron and some stainless steels, Chalmers University of Technology, 2007.
[38] J. Töpfer, S. Aggarwal, R. Dieckmann, Point defects and cation tracer diffusion in (CrxFe1 − x)3 − δO4 spinels, Solid State Ion. 81 (1995) 251–266.
[39] J.A. Van Orman, K.L. Crispin, Diffusion in oxides, reviews in mineralogy, Geochemistry 72 (2010) 757–825.
[40] R. Dieckmann, M. Hilton, T.O. Mason, Defects cation Diffus. Magn. (VIII): Migr. enthalpies iron impurity cations 91 (1987) 59–66.
[41] T. Jonsson, S. Canovic, F. Liu, H. Asteman, J.E. Svensson, L.G. Johansson, M. Halvarsson, Microstructural investigation of the effect of water vapour on the oxidation of alloy 353 MA in oxygen at 700 and 900°C, Mater. High. Temp. 22 (2005) 231–243.
[42] T. Gheno, D. Monceau, D.J. Young, Mechanism of breakaway oxidation of Fe–Cr and Fe–Cr–Ni alloys in dry and wet carbon dioxide, Corros. Sci. 64 (2012) 222–233.
[43] T. Gheno, D. Monceau, D.J. Young, Kinetics of breakaway oxidation of Fe–Cr and Fe–Cr–Ni alloys in dry and wet carbon dioxide, Corros. Sci. 77 (2013) 246–256.
[44] J. Robertson, M. Manning, Healing layer formation in Fe–Cr–Si ferritic steels, Mater. Sci. 5 (1989) 741–753.
[45] C. Pascal, V. Parry, E. Fedorova, M. Braccini, P. Chemelle, N. Meyer, D. Oquab, D. Monceau, Y. Wouters, M. Mantel, Breakaway oxidation of austenitic stainless steels induced by alloyed sulphur, Corros. Sci. 93 (2015) 100–108.
[46] A. Col, V. Parry, C. Pascal, Oxidation of a Fe–18Cr–8Ni austenitic stainless steel at 850°C in O2: microstructure evolution during breakaway oxidation, Corros. Sci. 114 (2017) 17–27.
[47] W.H. Bragg, The structure of the spinel group of crystals, Philos. Mag. Sci. 30 (1915) 305–315.
[48] X. Liang, Y. Zhong, S. Zhu, H. He, P. Yuan, J. Zhu, Z. Jiang, The valence and site occupancy of substituting metals in magnetite spinel structure Fe3−xMxO4 (M = Cr, Mn, Co and Ni) and their influence on thermal stability: An XANES and TG-DSC investigation, Solid State Sci. 15 (2013) 115–122.
[49] D. Whittle, G. Wood, D. Evans, D. Scully, Concentration profiles in the underlying alloy during the oxidation of iron-chromium alloys, Acta Metall. 15 (1967) 1747–1755.
[50] D. Young, J. Zurek, L. Singheiser, W. Quadakkers, Temperature dependence of oxide scale formation on high-Cr ferritic steels in Ar–H2–H2O, Corros. Sci. 53 (2011) 2131–2141.
[51] E. Essuman, G. Meier, J. Żurek, M. Hänsel, L. Singheiser, W. Quadakkers, Enhanced internal oxidation as trigger for breakaway oxidation of Fe–Cr alloys in gases containing water vapor, Scr. Mater. 57 (2007) 845–848.
[52] T.D. Nguyen, J. Zhang, D.J. Young, Effects of silicon and water vapour on corrosion of Fe–20Cr and Fe–20Cr–20Ni Alloys in CO_2 at 650 °C, Oxid. Met. 87 (2017) 541–573.
[53] N. Otsuka, Y. Shida, H.J.O.o.M. Fujikawa, Intern. -Extern. Transit. Oxid. Fe-Cr-Ni austenitic Stainl. Steels Steam. 32 (1989) 13–45.
[54] A.K. Chakraborty, Formation of silicon-aluminum spinel, J. Am. Ceram. Soc. 62 (1979) 120–124.
[55] L. Bindi, W.L. Griffin, W.R. Panero, E. Sirotkina, A. Bobrov, T. Irifune, Synthesis of inverse ringwoodite sheds light on the subduction history of Tibetan ophiolites, Sci. Rep. 8 (2018) 5457.
[56] Y.C. Malede, K.V. Dahl, M. Montgomery, F.B. Grumsen, J. Hald, Effect of service exposure on KCl corrosion attack of AISI 347H FG steel, J. Mater. Sci. 54 (2019) 13787–13809.
[57] Y.C. Malede, M. Montgomery, K.V. Dahl, J. Hald, Effect of microstructure on KCl corrosion attack of modified AISI 310 steel, Mater. High. Temp. 35 (2018) 243–254.
[58] T. Jonsson, N. Folkeson, M. Halvarsson, J.E. Svensson, L.G. Johansson, Microstructural investigation of the HCl-induced corrosion of the austenitic alloy 310S (52Fe26Cr19Ni) at 500 °C, Oxid. Met. 81 (2014) 575–596.
[59] J.P. Simon, High Temperature Corrosion Behavior in Biomass- and Waste-Fired Boilers - Insights into catastrophic corrosion and corrosion mitigation techniques, in: Chemistry and Chemical Engineering, Chalmers University of Technology, 2020.
[60] C.-C. Hsieh, W. Wu, Overview of intermetallic sigma, ISRN Metall. 2012 (2012), 732471.
[61] P. Duhaj, J. Ivan, E. Makovicky, Sigma-phase precipitation in austenitic steels, Iron Steel Inst. 206 (1968) 1245–1251.
[62] M.E. Wilms, V.J. Gadgil, J.M. Krougman, F.P. Ijsseling, The effect of σ-phase precipitation at 800°C on the corrosion resistance in sea-water of a high alloyed duplex stainless steel, Corros. Sci. 36 (1994) 871–881.
[63] H.D. Solomon, T. Devine Jr., Duplex stainless steels–a tale of two phases, Duplex Stainl. Steels (1982) 693–756.
[64] E. Folkhard, Welding metallurgy of stainless steels. & Business Media, Springer Science, 2012.